AIAA JOURNAL
Vol. 44, No. 7, July 2006

Wall Pressure Fluctuations in a Turbulent Boundary Layer over a Bump

Joongnyon Kim* and Hyung Jin Sung†
Korea Advanced Institute of Science and Technology, 373-1 Guseong-dong, Yuseong-gu, Daejeon 305-701, Republic of Korea

DOI: 10.2514/1.6519

Direct numerical simulations of a turbulent boundary layer over a bump were performed to examine the effects of surface longitudinal curvature on wall pressure fluctuations. Turbulence statistics and frequency spectra were examined to elucidate the response of wall pressure fluctuations to the longitudinal curvature and to the corresponding pressure gradient. Wall pressure fluctuations were significantly enhanced near the trailing edge of the bump, where the boundary layer is subjected to a strong adverse pressure gradient. Large-scale structures in the wall pressure fluctuation distribution were observed to grow rapidly near the trailing edge of the bump and convect downstream. In addition, the distance between the streamwise vortices and the wall increased slightly near the trailing edge of the bump. This caused the magnitude of the streamwise vorticity to increase significantly due to the diminishing of the interaction with the wall, leading to an enhancement of the wall pressure fluctuations.

Nomenclature

C_f	=	skin friction coefficient
C_p	=	mean wall pressure coefficient
k_z	=	spanwise wave number
P^+	=	pressure gradient parameter
p_w	=	wall pressure fluctuations
q_∞	=	reference dynamic pressure
R_{pp}	=	two-point correlation of wall pressure fluctuations
Re_θ	=	Reynolds number based on U_∞ and θ_0, $U_\infty\theta_0/\nu$
S	=	acoustic source
U_∞	=	freestream velocity
u_τ	=	friction velocity
θ_0	=	skin friction coefficient
ω	=	frequency

Subscripts

rms	=	root mean square value
w	=	values at the wall
$'$	=	fluctuating component
$+$	=	normalized by wall variables
$*$	=	complex conjugate

I. Introduction

KNOWLEDGE of wall pressure fluctuations is essential if we are to understand the dynamic behavior of wall turbulent flows and flow noise. One practical example in which such knowledge is vital is noise generation caused by the flow over a sonar transducer mounted on a ship or a submarine. In addition, unsteady pressure data play a fundamental role in the analysis of the sound radiated from a surface. To predict the acoustic pressure level based on Curle's solution [1] of the Lighthill equation, an accurate spatial distribution of wall pressure fluctuations is needed. Considerable experimental and theoretical work has been carried out with the aim of constructing a reliable spectral model of pressure fluctuations [2,3].

The majority of previous studies on wall pressure fluctuations have examined equilibrium turbulent boundary layers over flat plates or inside channels [4–6]. The experimental studies on wall pressure fluctuations have been reviewed by Willmarth [7] and Eckelmann [8]. Initial attempts at measuring wall pressure fluctuations were made difficult by problems associated with pressure transducers, which gave rise to poor spatial resolution and frequency response. Recently, however, Lee and Sung [9] managed to accurately measure the wall pressure fluctuations in flow over a backward-facing step using a multiple-arrayed measurement technique. Their findings revealed that there exist two modes of vortex shedding. Hudy et al. [10] also observed that the existence of self-sustained oscillations near the middle of the recirculation zone.

The difficulties involved in experimentally measuring wall pressure fluctuations can be avoided by using direct numerical simulations (DNS) [11–13]. Neves and Moin [14] examined the effects of convex transverse curvature on wall pressure fluctuations in axial flow boundary layers. They demonstrated that the rms pressure fluctuations decrease with increasing the transverse curvature of the surface. In addition, Na and Moin [15] studied the effects of a pressure gradient and separation on wall pressure fluctuations. They observed large two-dimensional roller-type structures inside the separation bubble. Recently, Kim et al. [16] investigated the characteristics of wall pressure fluctuations after the sudden application of wall blowing or suction. They showed that wall pressure fluctuations are more sensitive to blowing than to suction. In particular, for the system subjected to blowing, they observed large-scale elongated structures in the wall pressure fluctuation distribution near the location of maximum rms pressure fluctuations. However, the effects of longitudinal curvature on wall pressure fluctuations have yet to be established.

The main objective of the present study was, therefore, to investigate the effects of longitudinal curvature on wall pressure fluctuations. To achieve this, DNSs of a turbulent boundary layer over a bump were performed. The boundary layer over a bump has been widely studied due to its geometrical complexity, which involves both pressure gradients and surface curvature [17–19]. A schematic diagram of the flow geometry is shown in Fig. 1. The surface bump is defined by three tangential circular arcs. The boundary layer experiences a short region of concave surface, a longer region of convex surface, another short region of concave surface, and then returns to the flat plate. As a result of this geometry, the streamwise pressure gradient changes from adverse to favorable in the region upstream of the bump apex. Downstream of the bump apex, the boundary layer is subjected to an adverse pressure gradient before returning to a favorable pressure gradient over the flat plate.

Received 17 November 2003; revision received 13 December 2005; accepted for publication 7 March 2006.

*Department of Mechanical Engineering.
†Department of Mechanical Engineering; hjsung@kaist.ac.kr (corresponding author).

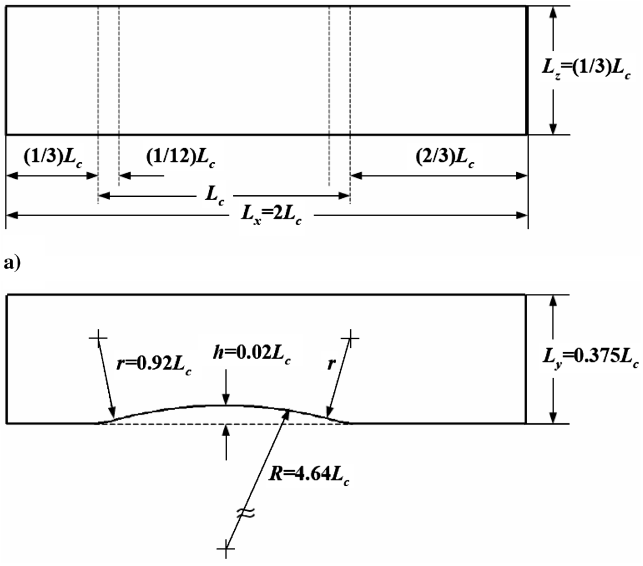

Fig. 1 Schematic diagram of the flow geometry: a) Top view of the computational domain; b) Side view of the computational domain.

Table 1 lists the bump parameters used in the present work, along with those used in previous studies on systems with a similar flow geometry. In the present DNS, we specified the bump parameters so that the streamwise distribution of the computed wall pressure coefficient matched that of Webster et al. [18] (Fig. 3a). Because the Reynolds number considered in the present DNS was smaller than in the previous studies, a smaller curvature parameter (δ/R) was used in the present work. However, taking into consideration the findings of Bradshaw [20], who demonstrated that a convex curvature of $\delta/R = 0.01$ significantly reduced the skin friction coefficient, the bump used in the present work was expected to have a significant effect on the turbulent boundary layer. The surface bump has two discontinuities in surface curvature: the concave-to-convex surface near the leading edge and the convex-to-concave surface near the trailing edge. Note that, at both of these discontinuities, the bump used in the present work has a value of $\Delta k^* = 5.52 \times 10^{-4}$, which satisfies the criterion of $\Delta k^* > 0.37 \times 10^{-4}$ for the formation of an "internal layer" [17]. Here, $\Delta k^* = (1/R_2 - 1/R_1)\nu/u_\tau$ where R_1 and R_2 are upstream and downstream radii of curvature, respectively.

Abrupt discontinuities in surface curvature are known to trigger internal layer formation. For example, in a study of the flow over a curved hill, a geometry similar to that considered here [17] observed the formation of an internal layer at the discontinuity in the surface curvature and the subsequent growth of this layer over the convex surface. The internal layer is shown by knee points in the profiles of turbulence intensity. Additionally, they found that the streamwise turbulence intensity is significantly larger in the internal layer than in the outer layer. Webster [18] observed that the change in surface curvature from convex to concave near the trailing edge of the bump triggers the formation of a second internal layer. They found that most of the flow behavior could be accounted for in terms of pressure gradient effects, indicating that the convex surface has only a small influence on the flow characteristics. Recently, Wu and Squires [19] suggested that the abrupt increase of skin friction caused by the presence of a pressure gradient enhances near-wall turbulence stresses and plays a key role in the formation of the internal layer.

The objective of the present study was to obtain a statistical description of the wall pressure fluctuations in the turbulent boundary layer over a bump, with particular emphasis on the response of wall pressure fluctuations to longitudinal curvature and the corresponding pressure gradient. Turbulence statistics and frequency spectra of wall pressure fluctuations were extracted using standard techniques for analyzing stochastic data. In addition, two-point correlation coefficients and coherence functions were used to deduce the spatial structure of the wall pressure fluctuations. The behavior of the wall pressure fluctuations with convection downstream is presented in terms of spatiotemporal correlations and convection velocities. A time sequence of instantaneous fields is visualized to investigate the evolution of the wall pressure fluctuations.

Table 1 Comparison of bump parameters

Case	δ/R	δ/h	h/R	$\Delta k^* \times 10^4$
Baskaran et al. [17]	0.052	0.27	0.19	0.516
Webster et al. [18]	0.06	1.5	0.04	2.9
Wu and Squires [19]	0.072	1.77	0.04	4.05
Present	0.015	3.0	0.005	5.52

II. Direct Numerical Simulation

For an incompressible flow, the nondimensional governing equations are

$$\frac{\partial u_i}{\partial t} + \frac{\partial}{\partial x_j} u_i u_j = -\frac{\partial p}{\partial x_i} + \frac{1}{Re}\frac{\partial}{\partial x_j}\frac{\partial u_i}{\partial x_j} \tag{1}$$

$$\frac{\partial u_i}{\partial x_i} = 0 \tag{2}$$

where x_i are the Cartesian coordinates and u_i are the corresponding velocity components. All variables are nondimensionalized by a characteristic length and velocity scale, and Re is the Reynolds number.

By introducing generalized coordinates η^i, the velocity components u_i are transformed into the volume fluxes across the faces of the cell q^i or $\mathbf{q}$. Formulation of the problem in terms of the contravariant velocity components, weighted with the Jacobian J in conjunction with the staggered variable configuration, leads to discretized equations. The transformed governing equations are rewritten as

$$\frac{\partial q^i}{\partial t} + N^i(q) = -G^i(p) + L_1^i(q) + L_2^i(q) \tag{3}$$

$$D^i q^i = \frac{1}{J}\left(\frac{\partial q^1}{\partial \eta^1} + \frac{\partial q^2}{\partial \eta^2}\right) + \frac{\partial q^3}{\partial \eta^3} = 0 \tag{4}$$

where N^i is the convective term, $G^i(p)$ is the pressure gradient term, L_1^i and L_2^i are the diffusion terms without and with cross derivatives, and D^i is the divergence operator. More details can be found in Choi et al. [21].

The governing equations are integrated in time by using a fully implicit, fractional-step method, which has been proposed by Choi and Moin [22]. The fractional step is a method of approximation of the governing equations based on the decomposition of the operators. In applying this method to the Navier–Stokes equations, we can interpret the role of pressure in the momentum equations as a projection operator, which projects an arbitrary vector field into a divergence-free vector. In Cartesian coordinates, the four steps are

$$\frac{\hat{u}_i - u_i^n}{\Delta t} + \frac{1}{2}\frac{\partial}{\partial x_j}(\hat{u}_i\hat{u}_j + u_i^n u_j^n) = -\frac{\partial p^n}{\partial x_i} + \frac{1}{2}\frac{1}{Re}\frac{\partial}{\partial x_j}\frac{\partial}{\partial x_j}(\hat{u}_i + u_i^n) \tag{5}$$

$$\frac{\breve{u}_i - \hat{u}_i}{\Delta t} = \frac{\partial p^n}{\partial x_i} \tag{6}$$

$$\frac{\partial}{\partial x_i}\frac{\partial p^{n+1}}{\partial x_i} = \frac{1}{\Delta t}\frac{\partial \breve{u}_i}{\partial x_i} \tag{7}$$

$$\frac{u_i^{n+1} - \breve{u}_i}{\Delta t} = -\frac{\partial p^{n+1}}{\partial x_i} \tag{8}$$

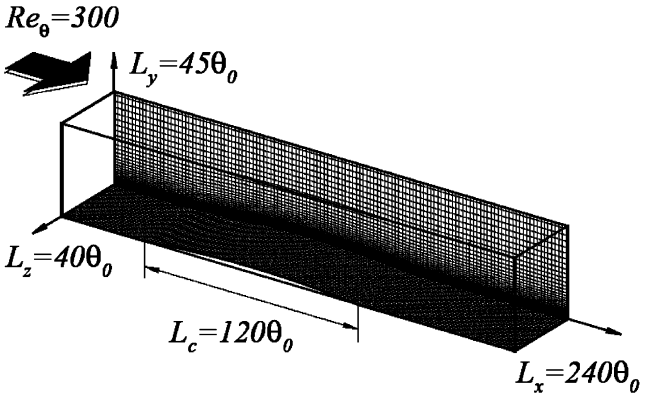

Fig. 2 Computational domain and grid system.

Table 2 Comparison of computational grid resolutions

Case	Δx^+	$\Delta y^+_{\min} \sim \Delta y^+_{\max}$	Δz^+
Kim et al. [23]	12.0	$0.05 \sim 4.4$	7.0
Lee et al. [24]	10.0	$0.3 \sim 31.0$	15.0
Na and Moin [15]	18.3	$0.11 \sim 22.7$	10.5
Present	12.5	$0.16 \sim 24.1$	5.0

A second-order central difference scheme is used for the spatial derivatives and a Crank–Nicolson method is employed in time advancement. Substitution of Eqs. (6) and (8) into Eq. (5) indicates that the present scheme is second-order accurate in time. The discretized nonlinear momentum equations are solved by using a Newton iterative method. Solving the Poisson equation for p satisfies the continuity equation. In this computation, Eqs. (5–8) are also transformed from Cartesian coordinates to the generalized coordinate.

Time-dependent turbulent inflow data are provided at the inlet based on the method by Lund et al. [25]. This approach is to extract instantaneous planes of velocity data from an auxiliary simulation of spatially developing turbulent boundary layer over a flat plate. A plane velocity field near the domain exit is modified by the rescaling procedure and reintroduced to the inlet of the computational domain in the inflow-generation simulation. The main simulation of a turbulent boundary layer over a bump is then carried out. A convective boundary condition at the exit has the form $(\partial u_i/\partial t) + c(\partial u_i/\partial x) = 0$, where c is the local bulk velocity. The no-slip boundary condition is imposed at the solid wall, and the boundary conditions on the top surface of the computational domain are $\partial u_1/\partial y = 0$, $u_2 = 0$, and $u_3 = 0$. A periodic boundary condition is applied in the spanwise direction.

Figure 2 shows a schematic diagram of the computational domain and grid system. The computational domain size in each direction is $L_x = 240$, $L_y = 45$, and $L_z = 40$, respectively. The inlet Reynolds number based on the inlet momentum thickness (θ_0) and freestream velocity (U_∞) was $Re = 300$. Nonuniform grid distributions are used in both the streamwise and wall-normal directions, and uniform grid distribution in the spanwise direction. The computational grid is generated using the direct distribution control technique by Thomas and Middlecoff [26]. Comparison of the computational grid resolution with the previous DNS is presented in Table 2. For all directions, the present resolution is everywhere comparable to or better than that of the previous DNS. The computational time step used is $\Delta t = 0.3\ \theta_0/U_\infty$ and the total averaging time to obtain the statistics is $T_{\text{avg}} = 5000\ \nu/u_\tau^2$, where ν and u_τ are the kinematic viscosity and the friction velocity, respectively. A streamline-normal coordinate system (s, n, z) was used for postprocessing, where the n axis is perpendicular to the lower surface in Fig. 1b. The corresponding velocity components in (s, n, z) are denoted (u_s, u_n, u_z). A normalized streamwise coordinate $x' = (x - x_0)/L_c$ was also used, where x_0 corresponds to the leading edge of the bump and L_c is the bump length. In the x'-coordinate system, $x' = 0$ coincides with the leading edge, $x' = 0.5$ with the bump apex and $x' = 1.0$ with the trailing edge.

III. Results and Discussion

A. Mean Wall Pressure and Flow Field

Figure 3a shows the wall pressure coefficients (C_p^*) calculated in the present work along with the experimental data of Webster et al. [18]. The form of $C_p^* = (C_p - C_{p,\min})/(C_p, \text{ref} - C_{p,\min})$ was utilized by Hudy et al. [10], who made a comparison of the mean pressure data in a separated and reattached flow. The present results are in excellent agreement with the experimental data. The behavior of the wall pressure coefficient C_p^* indicates that the boundary layer develops under a zero pressure gradient at the inlet and that the streamwise pressure gradient then becomes mildly adverse over the upstream flat plate. On moving downstream to the leading edge of the bump, the boundary layer experiences a short region of concave curvature followed by a region of convex curvature, with the corresponding pressure gradient changing from adverse to favorable. Downstream of the bump apex, the streamwise pressure gradient is initially strongly adverse and then changes to mildly favorable over the exit flat plate.

Figure 3b shows the distribution of the nondimensional pressure gradient parameter P^+, which is defined as

$$P^+ = \frac{\nu}{\rho u_\tau^3}\frac{d\langle p_w\rangle}{ds} \tag{9}$$

Here, the brackets indicate an average over the spanwise direction and time. P^+ changes sign at three streamwise locations, $x' = 0.038$, 0.52, and 1.04. Thus, according to the sign of the streamwise pressure gradient, the computational domain can be divided into four streamwise regions, specifically $-0.33 < x' < 0.038$ (region I), $0.038 < x' < 0.52$ (region II), $0.52 < x' < 1.04$ (region III), and $1.04 < x' < 1.67$ (region IV). Notably, in the range of $0.78 < x' < 1.02$ in region III, P^+ exceeds the value of 0.09 suggested by Patel as the threshold value above which separation processes occur [27]. Through the region $0.78 < x' < 1.02$, the boundary layer experiences intermittent reversal in the vicinity of the wall but remains attached on average.

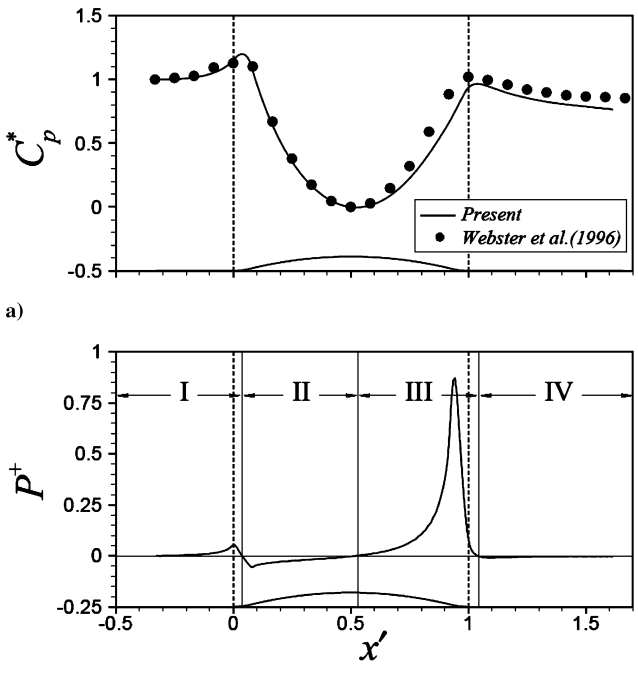

Fig. 3 a) Comparison of mean wall pressure with the experimental data; b) Streamwise distribution of pressure gradient parameter.

Figure 4 shows the streamwise distribution of the skin friction coefficient $C_f = \tau/(rU_\infty^2/2)$. Compared with the value at the inlet, C_f is lower when the boundary layer is subjected to an adverse pressure gradient (regions I and III), but higher when the boundary layer is subjected to a favorable pressure gradient (regions II and IV). On moving through the flat-to-concave transition in the surface, C_f increases rapidly at the region where the pressure gradient decreases. A similar rapid increase of C_f is observed near the trailing edge of the bump. As pointed out by Wu and Squires [19], this change in C_f can be regarded as evidence of internal layer generation at a curvature discontinuity. The overall distribution shown in Fig. 4 is similar to that measured experimentally by Baskaran et al. [17]. The local minimum of C_f at $x' = 0.94$ is due to the intermittent reverse flows near the trailing edge of the bump. The degree of intermittent reversal can be quantified by the intermittent factor $\gamma^+ = \Sigma t(u_{s,w} > 0)/\Sigma t$. Figure 4 presents the computed streamwise distribution of γ^+. Based on the previous result that intermittent detachment occurs when $\gamma^+ < 0.8$ (Wu and Squires [19]), we see that intermittent detachment occurs at $x' = 0.92$, the streamwise location of the convex-to-concave surface discontinuity, and that intermittent reattachment occurs at $x' = 1.0$, the streamwise location at which $(p_w)_{\rm rms}$ has a maximum value (shown in the next section).

Figure 5a depicts the instantaneous streamwise velocity distribution at the domain center, while Fig. 5b presents the mean streamwise velocity distribution obtained by averaging over the spanwise direction and time. In these contour plots, the contour levels range from 0.1 to 0.9 in increments of 0.1, with an additional contour level of 0.99, indicating the boundary layer thickness. The contours of streamwise turbulence intensity are illustrated in Fig. 5c, where the contour levels range from 0.01 to 0.17 in increments of 0.01. The instantaneous velocity field (Fig. 5a) clearly exhibits intermittent reverse flows near the bump trailing edge, but no separation zones are observed in the mean field (Fig. 5b). Note that the concave-to-convex curvature discontinuity triggers the formation of an internal layer, consistent with previous studies [17–19]. The streamwise turbulence intensity in the internal layer is significantly larger than that in the outer layer. On moving downstream to above the bump, the internal layer grows away from the wall (Fig. 5c). Thus, the present DNS results confirm the existence of the internal layer above the bump.

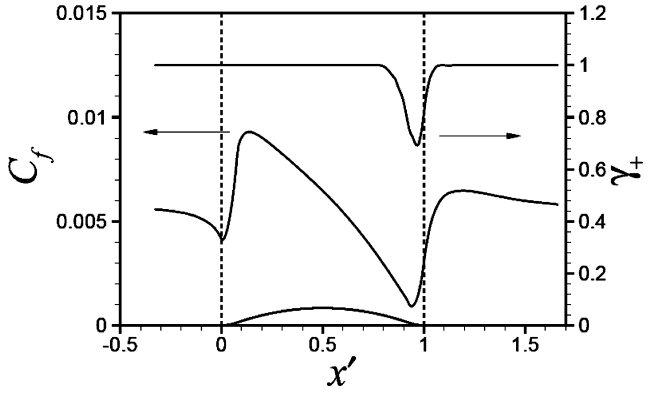

Fig. 4 Streamwise distribution of skin friction coefficient and intermittency factor.

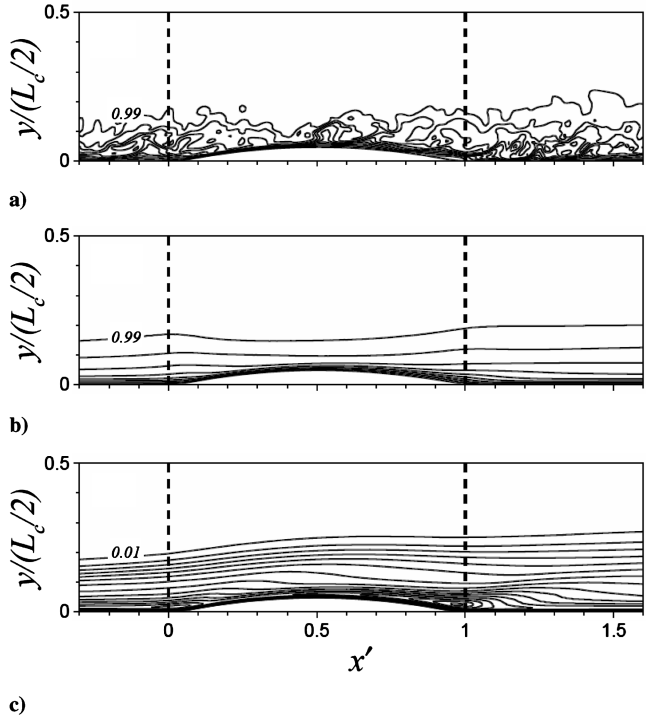

Fig. 5 Contour of a) instantaneous streamwise velocity; b) mean streamwise velocity; c) streamwise turbulence intensity.

B. One-Point Statistics of Wall Pressure Fluctuations

The streamwise distribution of rms wall pressure fluctuations $(p_w)_{\rm rms}$ normalized by the reference dynamic pressure $q_\infty = rU_\infty^2/2$ is shown in Fig. 6. Two peaks are observed, at $x' = 0.07$ and $x' = 1.0$, which correspond to surface locations close to the concave-to-convex and concave-to-flat transitions on the surface, respectively. With moving downstream of the bump apex, $(p_w)_{\rm rms}$ begins to increase near $x' = 0.78$, the location at which the pressure gradient parameter (P^+) exceeds 0.09. Since high-amplitude wall pressure fluctuations are closely linked with near-wall streamwise vortices and turbulent kinetic energy production [13], the activated streamwise vortices and turbulent fluctuations observed in region III may be the source of the observed increase of $(p_w)_{\rm rms}$ downstream of the apex.

To examine the spectral features of the wall pressure fluctuations, we calculated the frequency spectra of p_w using standard techniques for stochastic data. The wall pressure fluctuations $p_w(x, z, t)$ are Fourier-transformed in the spanwise direction and time. Letting $p_w(x, k_z, w)$ be the discrete Fourier transform of $p_w(x, z, t)$, the power spectral density is computed by

$$\Phi(k_z, \omega; x) = \langle \hat{p}_w(x, k_z, \omega)\hat{p}_w^*(x, k_z, \omega)\rangle \tag{10}$$

where * denotes the complex conjugate and the brackets indicate an average over the spanwise direction and time. The dependence on the streamwise location x is considered from the flow inhomogeneity. The frequency spectra $\varphi(\omega; x)$ are obtained by integrating $\Phi(k_z, \omega; x)$ over k_z. All spectra presented here are normalized such that their integral is equal to the mean-square of the wall pressure fluctuations.

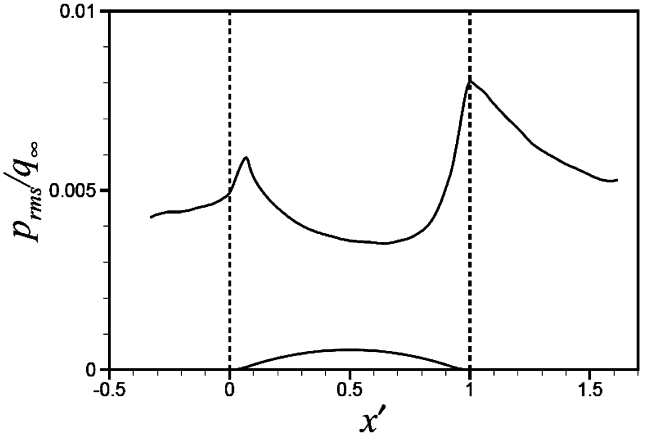

Fig. 6 Streamwise distribution of rms wall pressure fluctuations.

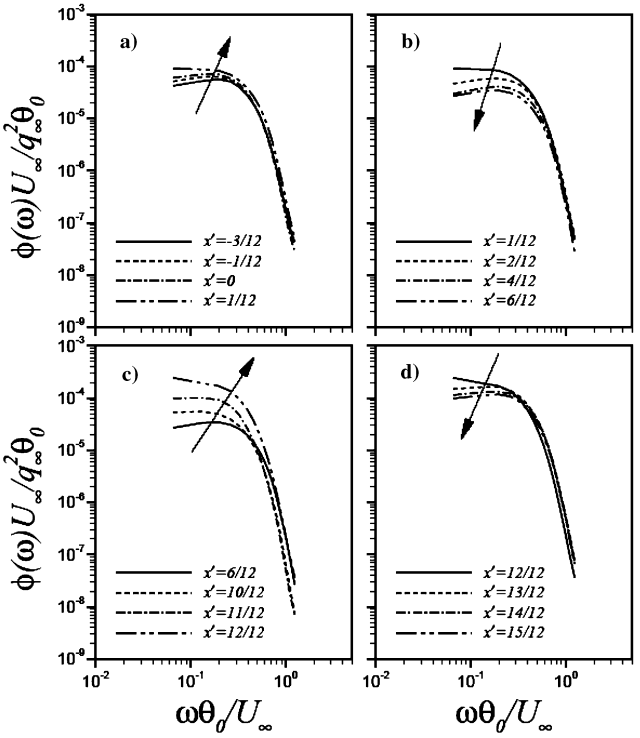

Fig. 7 Frequency spectra of wall pressure fluctuations with outer variable scaling: a) region I; b) region II; c) region III; d) region IV.

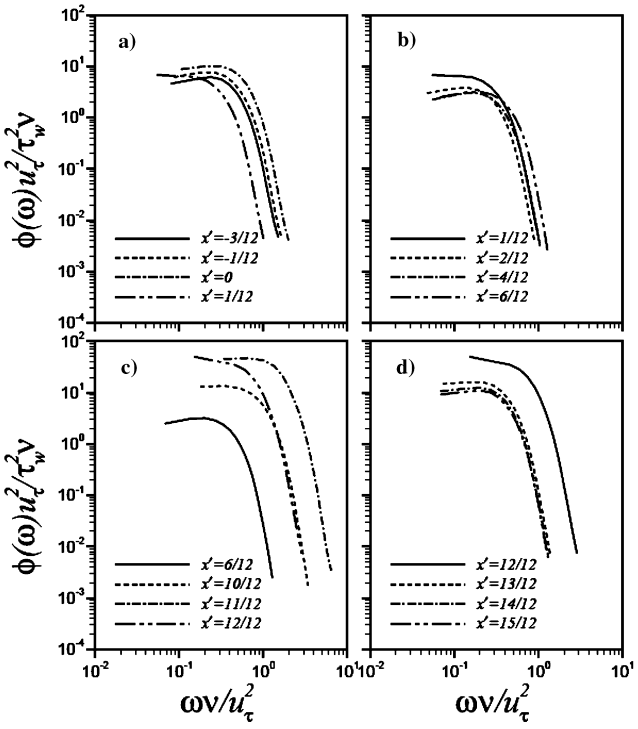

Fig. 8 Frequency spectra of wall pressure fluctuations with inner variable scaling: a) region I; b) region II; c) region III; d) region IV.

The spectra normalized by the outer variables are illustrated in Fig. 7. In all regions, the spectra collapse in the high frequency region. For $0.4 < \omega\ \theta_0/U_\infty$, the spectra decrease with a slope of approximately -5. The computed pressure spectra have a negligible region with a -1 slope, which arises from the contribution of motions in the logarithmic region. Closer inspection of Fig. 7 discloses that the power in the low-frequency region is the main determinant of the variation of $(p_w)_{\rm rms}$. For regions I and III, the spectra in the low-frequency region increase with increasing x' (Figs. 7a and 7c), indicating that the increase of large-scale power gives rise to the increase of $(p_w)_{\rm rms}$. For regions II and IV, the spectra in the low-frequency region decrease with increasing x' (Figs. 7b and 7d), indicating that the decrease of large-scale power produces the decrease of $(p_w)_{\rm rms}$.

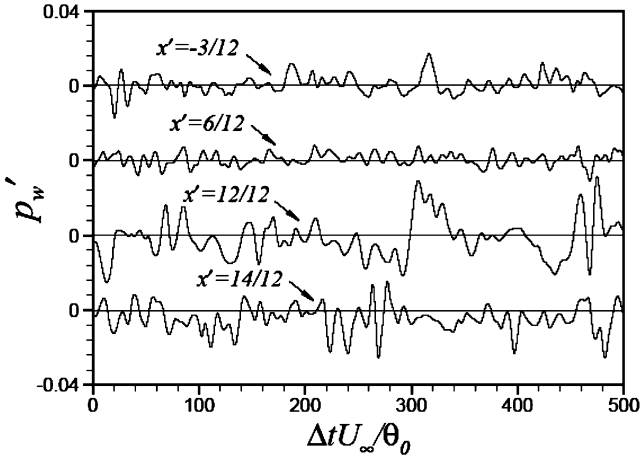

Fig. 9 Time history of wall pressure fluctuations.

The frequency spectra normalized by the inner variables are presented in Fig. 8. Owing to the different characteristics of the velocity and length scales, a reliable similarity scaling law is important for the comparison of frequency spectra. For all regions, the spectra scaled by the inner variables or the friction velocity u_τ do not converge in the high frequency region in the presence of a pressure gradient. As pointed out by Na and Moin [15], this is due to the fact that u_τ is no longer an important parameter in boundary layers with a pressure gradient.

Figure 9 shows the time evolution of wall pressure fluctuations at several streamwise locations, showing a wide range of time scale. In the boundary layer subjected to a strong adverse pressure gradient ($x' = 12/12$), the fluctuating frequency decreases slightly and the corresponding amplitude increases. At this location, the signal is dominated by low-frequency motions, indicating that large-scale structures grow in region III. From the one-point statistics and time history results presented above, we conclude that the large-scale structure of the wall pressure fluctuations plays a key role in determining the distribution of $(p_w)_{\rm rms}$ in all four regions. In particular, the large-scale structure grows rapidly in region III, where the boundary layer is subjected to a strong adverse pressure gradient.

C. Spatial Features of the Wall Pressure Fluctuations

The spatial characteristics of the wall pressure fluctuations are obtained from the two-point correlations as a function of the streamwise spatial (Δx) and temporal (Δt) separations,

$$R_{pp}(\Delta x, \Delta t; x) = \frac{\langle p_w(x, z, t) p_w(x + \Delta x, z, t + \Delta t)\rangle}{(p_w)_{\rm rms}(x, z, t)(p_w)_{\rm rms}(x + \Delta x, z, t + \Delta t)} \tag{11}$$

where the brackets indicate an average over the spanwise direction and time. Again, the dependence on the streamwise location x is considered from the flow inhomogeneity. The contours of the two-point correlation are presented in Fig. 10 for six streamwise locations. In these plots, the contour levels range from 0.1 to 0.9 in increments of 0.1. For the purpose of comparison, the spatial separations are normalized by the inlet momentum thickness. The strong convective nature of the wall pressure fluctuations is evidenced by the concentration of the contours into a band. A slight increase in the slope of $\Delta x/\Delta t$ indicates that the convection velocity of large eddies is higher than that of small eddies. From Fig. 10, it is clear that the wall pressure field loses coherence as con-

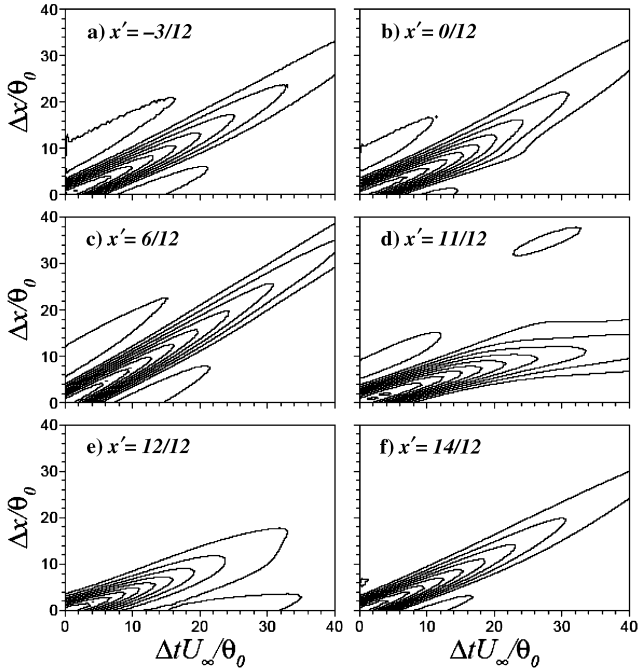

Fig. 10 Two-point correlation coefficient of wall pressure fluctuations as a function of streamwise spatial and temporal separations: a) $x' = -3/12$; b) $x' = 0/12$; c) $x' = 6/12$; d) $x' = 11/12$; e) $x' = 12/12$; f) $x' = 14/12$.

vection proceeds such that, when the flow has reached $x' = 11/12$ (Fig. 10d), the contour plot exhibits a curved shape, indicating that the wall pressure fluctuations do not proceed further downstream. Furthermore, the correlation decays rapidly at the trailing edge of the bump (Fig. 10e), indicating that the streamwise integral length scale of the wall pressure fluctuations decreases in region III, where the boundary layer is subjected to a strong adverse pressure gradient.

The convection velocities are calculated using the following definitions:

$$U_c(\Delta x) = \frac{\Delta x}{\Delta t_{\max}} \tag{12}$$

where $\Delta t_{\max}$ is the temporal separation for which R_{pp} is maximum at a given Δx, and

$$U_c(\Delta t) = \frac{\Delta x_{\max}}{\Delta t} \tag{13}$$

where $\Delta x_{\max}$ is the streamwise separation for which R_{pp} is maximum at a given Δt. The computed convection velocities normalized by the freestream velocity are presented in Fig. 11. At the leading edge of the bump, the convection velocity of large scales, corresponding to large separations in space or time, is approximately $0.8U_\infty$ and that of small scales is approximately $0.6U_\infty$. At the bump apex ($x' = 6/12$), the convection velocity has a maximum value of $0.8U_\infty$ and the convection velocity of large scales is nearly the same as that of small scales. At the trailing edge of the bump $x' = 12/12$ the wall pressure fluctuations have the smaller convection velocity of $0.4 \sim 0.5U_\infty$. It is seen in Fig. 11 that U_c decreases when the boundary layer is subjected to an adverse pressure gradient, but increases under a favorable pressure gradient.

Figure 12 shows the two-point correlation of wall pressure fluctuations as a function of the spanwise spatial and temporal separations,

$$R_{pp}(\Delta z, \Delta t; x) = \frac{\langle p_w(x, z, t) p_w(x, z + \Delta z, t + \Delta t) \rangle}{(p_w)_{\rm rms}(x, z, t)(p_w)_{\rm rms}(x, z + \Delta z, t + \Delta t)} \tag{14}$$

where the brackets indicate an average over the spanwise direction and time. The contour levels range from 0.1 to 0.9 in increments of

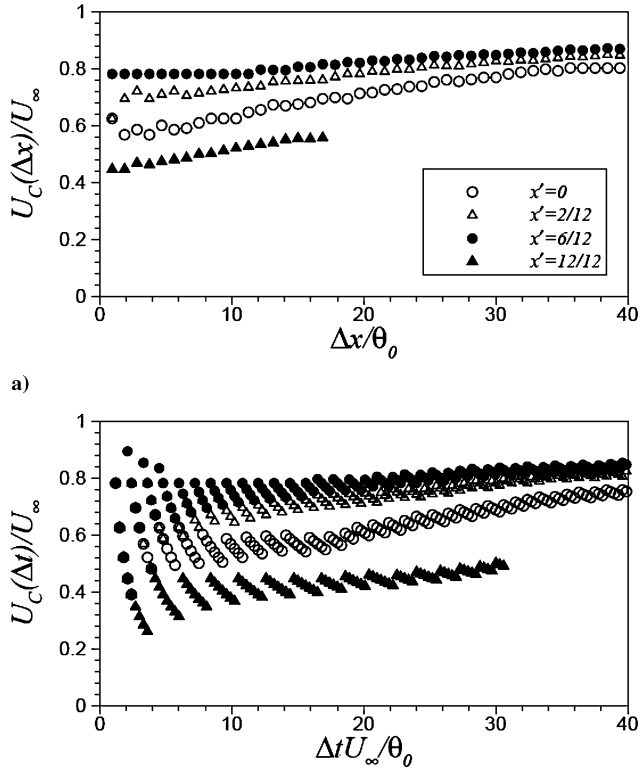

Fig. 11 Convection velocities as a function of: a) streamwise separation; b) temporal separation.

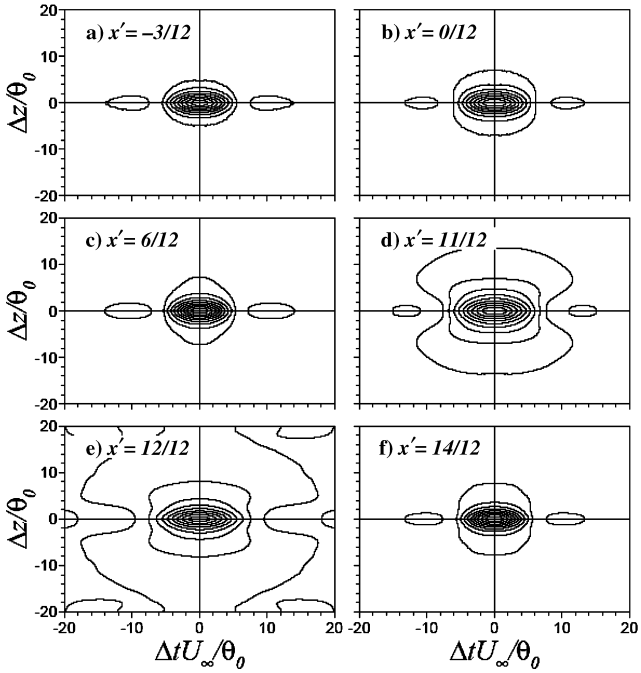

Fig. 12 Two-point correlation coefficient of wall pressure fluctuations as a function of spanwise spatial and temporal separations: a) $x' = -3/12$; b) $x' = 0/12$; c) $x' = 6/12$; d) $x' = 11/12$; e) $x' = 12/12$; f) $x' = 14/12$.

0.1. Near the trailing edge of the bump, the contours become elongated at larger separations in the spanwise direction (Figs. 12d and 12e). The spanwise extent of the widest contour (the contour level 0.1) increases up to $x' = 12/12$, where $(p_w)_{\rm rms}$ takes on a maximum value. This indicates that the spanwise integral length scale of wall pressure fluctuations increases in region III. These

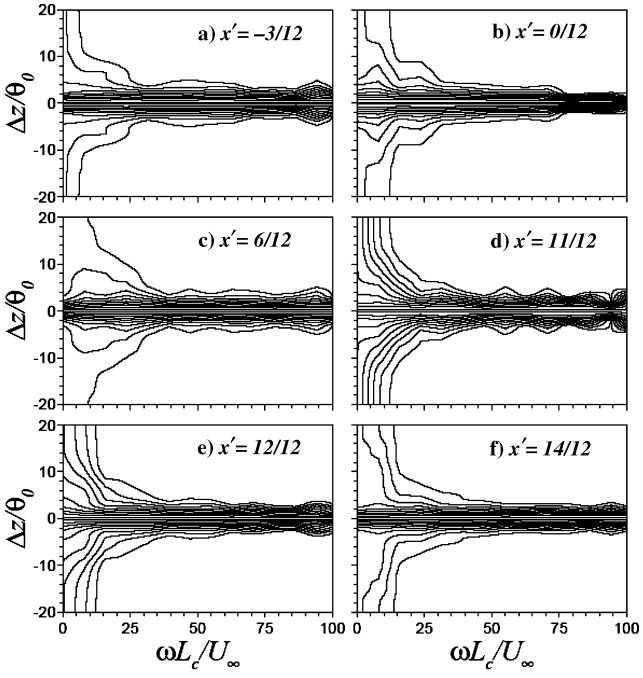

Fig. 13 Contours of coherence function: a) $x' = -3/12$; b) $x' = 0/12$; c) $x' = 6/12$; d) $x' = 11/12$; e) $x' = 12/12$; f) $x' = 14/12$.

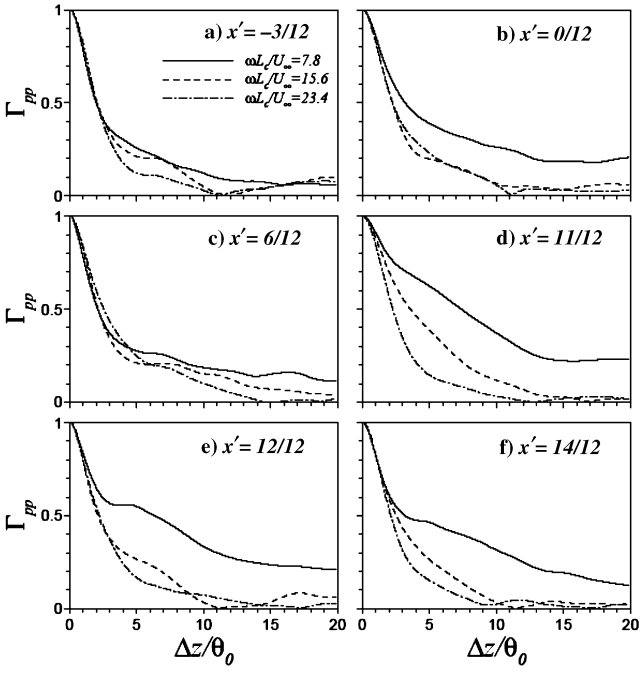

Fig. 14 Coherence function in low frequencies: a) $x' = -3/12$; b) $x' = 0/12$; c) $x' = 6/12$; d) $x' = 11/12$; e) $x' = 12/12$; f) $x' = 14/12$.

correlation coefficient results are consistent with the presence of a quasi-two-dimensional structure of wall pressure fluctuations near the trailing edge of the bump. This quasi-two-dimensional structure arises due to the strengthened vortical structure, which produces wall-normal motions in the buffer region and the spanwise spread beneath the viscous sublayer [16].

To quantify the change in the pressure field over the distance $\Delta \boldsymbol{x}$ we consider a normalized magnitude of the cross spectrum. The function, termed the coherence $\Gamma_{pp}(\Delta \boldsymbol{x}, \omega; x)$, is defined as

$$\Gamma_{pp}(\Delta x, \omega; x) = \frac{|\Phi(\Delta x, \omega; x)|}{[\phi(\omega; x)\phi(\omega; x + \Delta x)]^{1/2}} \qquad (15)$$

where the cross spectrum function $\Phi(\Delta \boldsymbol{x}, w; x)$ is the Fourier transform of the space-time cross correlation function,

$$\Phi(\Delta x, \omega; x) = \int_{-\infty}^{\infty} R_{pp}(\Delta x, \Delta t; x) e^{-j\omega(\Delta t)}\, \mathrm{d}(\Delta t) \qquad (16)$$

Figure 13 shows contour plots of the spanwise coherence $\Gamma_{pp}(\Delta z, \omega; x)$ at six streamwise locations. The coherence decreases rapidly with spanwise separation, except in the low-frequency region. In particular, the coherence in the low-frequency region intensifies significantly near the trailing edge of the bump, where a strong adverse pressure gradient is present (Figs. 13d and 13e). The behavior of the spanwise coherence provides further evidence of the growth of large-scale motions corresponding to the low-frequency motions, and shows that, in region III, where the boundary layer is subjected to a strong adverse pressure gradient, these large-scale structures grow rapidly.

To further explore the observed rapid decrease in the coherence with spanwise separation, except in the low-frequency region, in Fig. 14 we depict Γ_{pp} at selected low frequencies. For $\omega L_c/U_\infty > 15.6$, the coherence exhibits sufficient decrease within the computational domain. Hence, the total noise spectrum for these frequencies is the summation of the contributions from independent source regions [28]. At low frequency ($\omega L_c/U_\infty = 7.8$), the coherence length near the trailing edge of the bump is larger than the spanwise dimension of the computational domain and hence the total noise cannot be determined with certainty.

D. Instantaneous Pressure Field

To directly observe the growth of the large-scale structures near the trailing edge of the bump, we generated a time sequence of instantaneous flow fields. Figure 15 shows contour plots of the spanwise-averaged wall pressure fluctuations at times $tU_\infty/\theta_0 = 0$, 3, 6, and 9. The difference in eddy length scales between upstream and downstream of the bump apex is evident in these plots. Downstream of the bump apex, large-scale structures rapidly grow and the resulting quasi-two-dimensional structures convect downstream. The intermittent reverse flows near the trailing edge of the bump are attributed to the passage of these large-scale structures.

Figure 16 represents the variations of rms streamwise vorticity fluctuations ω_s. These data show that the streamwise vorticity fluctuations are stronger downstream of the bump apex (Fig. 16b) than upstream (Fig. 16a). Furthermore, the location of the local maximum of ω_s moves away from the wall close to the trailing edge of the bump, indicating a slight increase in the distance between the streamwise vortices and the wall. Hence, the magnitude of ω_s

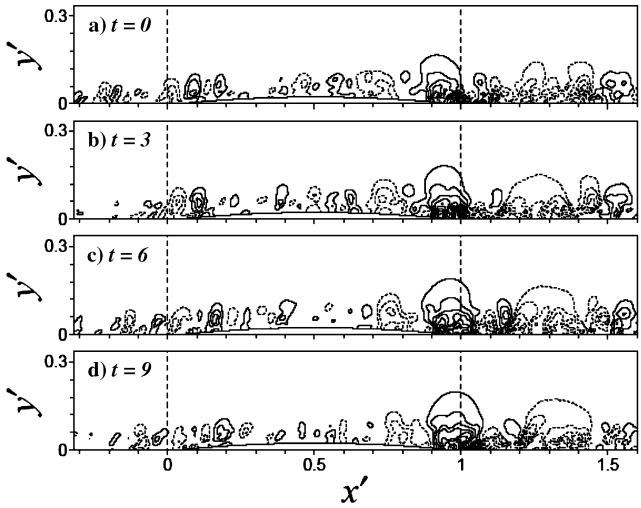

Fig. 15 Contours of spanwise-averaged pressure fluctuations in the x–y plane: a) $tU_\infty/\theta_0 = 0$; b) $tU_\infty/\theta_0 = 3$; c) $tU_\infty/\theta_0 = 6$; d) $tU_\infty/\theta_0 = 9$.

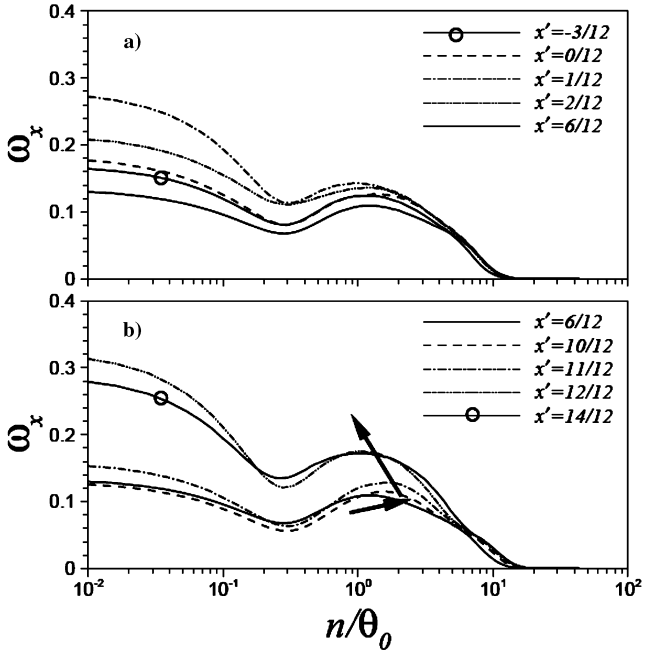

Fig. 16 Variations of streamwise vorticity fluctuations: a) upstream of the bump apex; b) downstream of the bump apex.

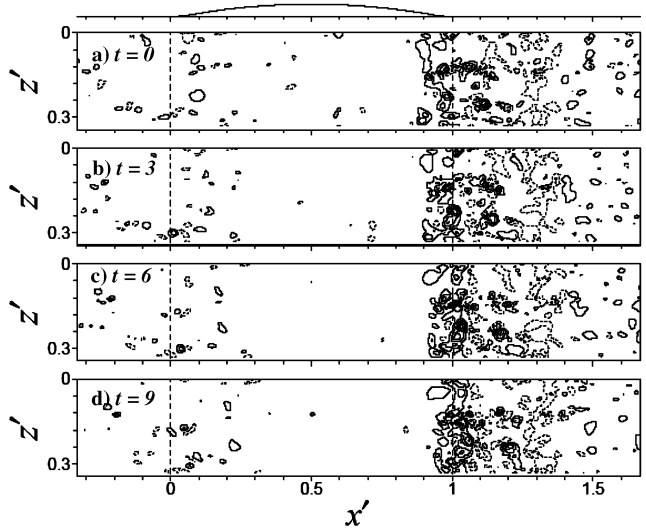

Fig. 17 Contours of wall pressure fluctuations in the x–z plane: a) $tU_\infty/\theta_0 = 0$; b) $tU_\infty/\theta_0 = 3$; c) $tU_\infty/\theta_0 = 6$; d) $tU_\infty/\theta_0 = 9$.

increases significantly due to the diminishing of the interaction with the wall. The maximum value of ω_s is observed at $x' = 12/12$, the streamwise location at which $(p_w)_{\rm rms}$ takes on a maximum value. This suggests that the magnitude of ω_s increases near the trailing edge of the bump, thereby causing an increased level of wall pressure fluctuations [11,13].

Finally, we consider the time evolution of the wall pressure fluctuations in the x–z plane. Figure 17 shows contour plots of the wall pressure fluctuations at the same times as in Fig. 15. In these plots, the wall pressure fluctuations are significantly enhanced near the trailing edge of the bump, where the boundary layer is subjected to a strong adverse pressure gradient. The large-scale structures in the wall pressure fluctuation distribution grow rapidly near the trailing edge of the bump and convect downstream. As these large-scale structures propagate downstream, they lose their coherence. We attribute the enhancement of the wall pressure fluctuations near the trailing edge of the bump to the growth of large-scale motions and the passage of quasi-two-dimensional structures.

IV. Conclusions

A detailed numerical analysis has been performed to scrutinize the effects of longitudinal curvature of a wall on the wall pressure fluctuations. Statistical descriptions of wall pressure fluctuations were obtained by direct numerical simulation of the turbulent boundary layer over a bump defined by three tangential circular arcs. Upstream of the bump apex, the streamwise pressure gradient changed from adverse to favorable with moving downstream. Downstream of the bump apex, the boundary layer was first subjected to an adverse pressure gradient before returning to a favorable pressure gradient over the flat plate. It was found that large-scale wall pressure fluctuations play a key role in determining the distribution of the rms wall pressure fluctuations $[(p_w)_{\rm rms}]$. The wall pressure fluctuations are significantly enhanced near the trailing edge of the bump, where the boundary layer is subjected to a strong adverse pressure gradient. In addition, large-scale structures in the wall pressure fluctuation distribution grow rapidly near the trailing edge of the bump and convect downstream. The appearance of intermittent reverse flows near the trailing edge of the bump is attributed to the passage of these large-scale structures. As the large-scale structures propagate downstream, they lose their coherence. Near the trailing-edge of the bump, the distance between the streamwise vortices and the wall increases slightly and thus the magnitude of the rms streamwise vorticity fluctuations increases significantly due to the diminishing of the interaction with the wall. The maximum value of streamwise vorticity is observed at $x' = 12/12$, the streamwise location at which $(p_w)_{\rm rms}$ takes on a maximum value.

Acknowledgement

The authors would like to acknowledge the support from KISTI (Korea Institute of Science and Technology Information) under "The Sixth Strategic Supercomputing Support Program." The use of the computing system of the Supercomputing Center is also greatly appreciated.

References

[1] Curle, N., "The Influence of Solid Boundaries upon Aerodynamic Sound," *Proceedings of the Royal Society of London A*, Vol. 231, No. 1187, 1955, pp. 505–514.

[2] Corcos, G. M., "The Structure of the Turbulent Pressure Field in Boundary-Layer Flow," *Journal of Fluid Mechanics*, Vol. 18, 1964, pp. 353–378.

[3] Blake, W. K., *Mechanics of Flow-induced Sound and Vibration*, Academic Press, Inc., 1986.

[4] Willmarth, W. W., "Wall Pressure Fluctuations in a Turbulent Boundary Layer," *Journal of the Acoustical Society of America*, Vol. 28, No. 6, 1956, pp. 1048–1053.

[5] Schewe, G., "On the Structure and Resolution of Wall-Pressure Fluctuations Associated with Turbulent Boundary-Layer Flow," *Journal of Fluid Mechanics*, Vol. 134, 1983, pp. 311–328.

[6] Farabee, T. M., and Casarella, M. J., "Spectral Features of Wall Pressure Fluctuations Beneath Turbulnet Boundary Layers," *Physics of Fluids A*, Vol. 3, No. 10, 1991, pp. 2410–2420.

[7] Willmarth, W. W., "Pressure Fluctuations Beneath Turbulent Boundary Layers." *Annual Review of Fluid Mechanics*, Vol. 7, 1975, pp. 13–38.

[8] Eckelmann, H., "A Review of Knowledge on Pressure Fluctuations," *Near Wall Turbulence: Proceedings of the 1988 Zoran Zaric Memorial Conference*, edited by S. J. Kline and N. H. Afgan, Hemisphere, New York, 1990, pp. 328–347.

[9] Lee, I., and Sung, H. J., "Multiple-Arrayed Pressure Measurement Toward the Investigation of the Unsteady Flow Structure of a Reattaching Shear Layer over a Backward-Facing Step," *Journal of Fluid Mechanics*, Vol. 463, 2002, pp. 377–402.

[10] Hudy, L. M., Naguib, A. M., and Humphreys, W. M., "Wall Pressure Array Measurements Beneath a Separating/Reattaching Flow Region," *Physics of Fluids*, Vol. 15, No. 3, 2003, pp. 706–717.

[11] Kim, J., "On the Structure of Pressure Fluctuations in Simulated Turbulent Channel Flow," *Journal of Fluid Mechanics*, Vol. 205, 1989, pp. 421–451.

[12] Choi, H., and Moin, P., "On the Space-Time Characteristics of Wall-

Pressure Fluctuations," *Physics of Fluids A*, Vol. 2, No. 8, 1990, pp. 1450–1460.
[13] Kim, J., Choi, J.-I., and Sung, H. J., "Relationship Between Wall Pressure Fluctuations and Streamwise Vortices in a Turbulent Boundary Layer," *Physics of Fluids*, Vol. 14, No. 2, 2002, pp. 898–901.
[14] Neves, J. C., and Moin, P., "Effects of Convex Transverse Curvature on Wall-Bounded Turbulence. Part 2: The Pressure Fluctuations," *Journal of Fluid Mechanics*, Vol. 272, 1994, pp. 383–406.
[15] Na, Y., and Moin, P., "The Structure of Wall-Pressure Fluctuations in Turbulent Boundary Layers with Adverse Pressure Gradient and Separation," *Journal of Fluid Mechanics*, Vol. 77, 1998, pp. 347–373.
[16] Kim, J., Kim, K., and Sung, H. J., "Wall Pressure Fluctuations in a Turbulent Boundary Layer After Blowing or Suction," *AIAA Journal*, Vol. 41, No. 9, 2003, pp. 1697–1704.
[17] Baskaran, V., Smits, A. J., and Joubert, P. N., "A Turbulent Flow over a Curved Hill. Part 1: Growth Of An Internal Boundary Layer," *Journal of Fluid Mechanics*, Vol. 182, 1987, pp. 47–83.
[18] Webster, D. R., DeGraaff, D. B., and Eaton, J. K., "Turbulence Characteristics of a Boundary Layer over a Two-Dimensional Bump," *Journal of Fluid Mechanics*, Vol. 320, 1996, pp. 53–69.
[19] Wu, X., and Squires, K. D., "Numerical Investigation of the Turbulent Boundary Layer over a Bump," *Journal of Fluid Mechanics*, Vol. 362, 1998, pp. 229–271.
[20] Bradshaw, P., "Effects of Streamline Curvature on Turbulent Flow," AGARD, AGARDograph, 169, 1973.
[21] Choi, H., Moin, P., and Kim, J., "Direct Numerical Simulation of Turbulent Flow Over Riblets," *Journal of Fluid Mechanics*, Vol. 255, 1993, pp. 503–539.
[22] Choi, H., and Moin, P., "Effects of the Computational Time Step on Numerical Solutions of Turbulent Flow," *Journal of Computational Physics*, Vol. 113, No. 1, 1994, pp. 1–4.
[23] Kim, J., Moin, P., and Moser, R., "Turbulence Statistics in Fully Developed Channel Flow at Low Reynolds Number," *Journal of Fluid Mechanics*, Vol. 177, 1987, pp. 133–166.
[24] Le, H., Moin, P., and Kim, J., "Direct Numerical Simulation of Turbulent Flow over a Backward-Facing Step," *Journal of Fluid Mechanics*, Vol. 330, 1997, pp. 349–374.
[25] Lund, T. S., Wu, X., and Squires, K. D., "Generation of Turbulent Inflow Data for Spatially-Developing Boundary Layer Simulations," *Journal of Computational Physics*, Vol. 140, No. 2, 1998, pp. 233–258.
[26] Thomas, P. D., and Middlecoff, J. F., "Direct Control of the Grid Point Distribution in Meshes Generated by Elliptic Equations," *AIAA Journal*, Vol. 18, No. 6, 1980, pp. 652–656.
[27] Patel, V. C., "Calibration of the Preston Tube and Limitations on Its Use in Adverse Pressure Gradients," *Journal of Fluid Mechanics*, Vol. 23, 1965, pp. 185–208.
[28] Wang, M., Lele, S. K., and Moin, P., "Computation of Quadrupole Noise Using Acoustic Analogy," *AIAA Journal*, Vol. 34, No. 11, 1996, pp. 2247–2254.

K. Ghia
Associate Editor